Heat storage performance analysis and parameter design for encapsulated phase change materials

Yu, Qinghua; Romagnoli, Alessandro; Al-Duri, Bushra; Xie, Danmei; Ding, Yulong; Li, Yongliang

DOI:
10.1016/j.enconman.2017.12.040

Document Version
Peer reviewed version

Citation for published version (Harvard):
Yu, Q, Romagnoli, A, Al-Duri, B, Xie, D, Ding, Y & Li, Y 2018, 'Heat storage performance analysis and parameter design for encapsulated phase change materials', *Energy Conversion and Management*, vol. 157, pp. 619-630. https://doi.org/10.1016/j.enconman.2017.12.040

Heat storage performance analysis and parameter design for encapsulated phase change materials

Qinghua Yu [a,b], Alessandro Romagnoli [c], Bushra Al-Duri [a], Danmei Xie [b], Yulong Ding [a], Yongliang Li [a,*]

[a] Birmingham Centre for Energy Storage, School of Chemical Engineering, University of Birmingham, Birmingham B15 2TT, United Kingdom

[b] School of Power and Mechanical Engineering, Wuhan University, Wuhan 430072, PR China

[c] School of Mechanical and Aerospace Engineering, Nanyang Technological University, Singapore 639798, Singapore

[*]Corresponding author. Tel.: +44 (0) 121 414 5135, Email: y.li.1@bham.ac.uk (Y. Li)

Abstract

This paper establishes a thermo-mechanical model considering the liquid density variation to explore the comprehensive energy storage performance of two types of small-sized encapsulated phase change materials (PCMs) as well as effects of shell thickness. The study shows that the varying ranges of internal pressure, melting temperature and latent heat are markedly diminished during melting of PCMs after taking into account the liquid density variation. The decrease of shell thickness leads to a decrease of maximum internal pressure and a larger decrease of critical cracking pressure, which will increase the risk of shell cracking. The decrease in shell thickness slows down the increase in melting temperature and the decrease in latent heat during the melting process, which consequently reduces the melting time and increases the stored latent energy. These results indicate that reducing shell thickness of encapsulated PCMs is favourable for elevating energy charging rate and energy storage capacity while it is harmful to mechanical stability. The Cu/Ni capsule has smaller critical core/shell size ratio to avoid cracking than the salts/SiC capsule, while the former offers a shorter melting period. This implies that physical properties of materials of PCM capsules should be carefully considered for improving mechanical stability and melting dynamics. This study is helpful for selection of appropriate shell thickness and materials to achieve excellent comprehensive energy storage performance of encapsulated PCMs.

Keywords: Phase change materials; Encapsulation; Melting; Thermal energy storage.

Nomenclature

Roman letters

a	shell thickness (m)
c_p	specific heat ($J \cdot kg^{-1} \cdot K^{-1}$)
E	Young's modulus (Pa)
ES	stored energy (J)
f	fraction
g	Gibbs free energy ($kJ \cdot kg^{-1}$)
h	enthalpy ($kJ \cdot kg^{-1}$)
L	latent heat ($kJ \cdot kg^{-1}$)
P	pressure (Pa)
r	radius (m)
s	entropy ($J \cdot kg^{-1} \cdot K^{-1}$)
t	time (s)
T	temperature (K)
u	displacement (m)
V	volume (m^3)

Greek letters

α	thermal expansion coefficient (K^{-1})
β	isothermal compressibility (Pa^{-1})
γ	heating rate ($^{\circ}C \cdot min^{-1}$)
δ, μ	Lamé's constant
λ	thermal conductivity ($W \cdot m^{-1} \cdot K^{-1}$)
ν	Poisson's ratio
ρ	density ($kg \cdot m^{-3}$)
σ	stress (Pa)
φ	relaxation factor

Subscripts

0	reference or initial
c	shell
e	external surface of shell
eq	equivalent
i	shell/PCM interface or PCM
l	liquid
m	melting or melting front
r, θ, φ	spherical coordinates system
s	solid
t	tensile strength

Superscripts

$*$	holistic

1. Introduction

High-temperature thermal energy storage (HTTES) provides an effective solution to overcome the mismatch between energy supply and demand associated with concentrated solar power generation [1, 2] and industrial waste heat recovery [3]. HTTES is also crucial to the round-trip efficiency enhancement of recently developed compressed air energy storage [4-6] and liquid air energy storage systems [7, 8]. Latent heat storage-based solid-liquid transition of phase change materials (PCMs) has attracted increasing attention because of high energy storage densities with small temperature variations [9]. However, the applicable PCMs for HTTES, such as molten salts and metals, exhibit high chemical corrosion in the liquid phase. Therefore it is essential to encapsulate PCMs in suitable shell materials to prevent leakage of liquid PCMs. The encapsulation of PCMs can also significantly increase heat transfer surface area and establish barriers for PCMs against harmful reactions with the environment [10]. The formed spherical PCM capsules offer stable geometric and chemical structures like solid balls or particles, which are easy to handle.

The spherical PCM capsules can be used for thermal energy storage in the form of packed beds [11, 12] or fluidized beds [13, 14]. The diameters of the PCM capsules used in packed beds generally measure tens of millimetres [15]. This kind of large-sized capsule is fabricated by filling in a precast container (i.e. shell) with PCM [16]. There will be some void or porosity inside this kind of capsule [17]. In contrast, the diameters of the capsules used in fluidized beds generally measure a few millimetres or hundreds of micrometres [18, 19]. This kind of small-sized capsule is manufactured by coating or plating PCM pellets with shell materials, which does not introduce voids inside the capsule [20, 21]. In comparison with packed beds, fluidized beds offer more advantages including temperature uniformity along the bed and excellent heat transfer between the carrier fluid and the PCM. However, since small-sized capsules have no voids inside, shell cracking may occur due to volume expansion

during phase transition of PCM from solid to liquid and this has to be considered in the design of PCM capsules [22]. Mathur et al. [23] developed PCM capsules tolerating PCM volume expansion by incorporating sacrificial polymer as the first shell layer which decomposes below the melting point of PCM to gas leaving a void in the capsule. Obviously, the resulting void layer reduces the heat storage density and charging/discharging rate. Zhang et al. [24] examined encapsulation of copper (Cu) as PCM with a thick chromium-nickel (Cr-Ni) bilayer. The results showed that there was no leakage or crack from the outside view of the capsule after charge-discharge thermal cycles. However, the integrity of the capsule is attributed to a sufficiently thick shell, which leads to a reduction of heat storage density by 70% with respect to the pure copper. Further, the shell thickness has considerable impact on the melting dynamics of PCM, which is closely related to the energy charging rate. Therefore, it is crucial to precisely tailor the shell thickness of PCM capsules to obtain excellent comprehensive heat storage performance, including good mechanical stability (i.e. no cracking), high heat storage density and fast charging/discharging processes.

Since it is difficult to directly measure the thermal and mechanical parameters within encapsulated PCMs, especially at high temperature, numerical simulation or analysis has become a very powerful tool. Several researchers have explored the heat storage performance of encapsulated PCMs for HTTES by numerical method. Zhao et al. [25] compared the charging/discharging time for encapsulated PCMs between different heat transfer fluids using numerical simulations of heat transfer regardless of volume variation. Lopez et al. [26] established a model for a solid sphere of PCM salts encapsulated in an elastic graphite shell with a mobile internal wall and a fixed external wall to explain the behaviour of graphite/salt composites during melting. The pressure inside the shell increases linearly as melting continues, leading to a continuous increase in the melting point and continuous decrease in latent heat. Pitié et al. [27] incorporated Lamé equations into the model to describe the

thermo-mechanical behaviour of a spherical PCM coated by silicon carbide (SiC) shell with a free, mobile, external wall by specifying volume friction of melted salts. The analysis indicates that the coated PCM with a low volumetric expansion resulting in a small pressure change is vital to avoid cracking. Parrado et al. [28] analysed the temperature and pressure evolutions during the melting and solidification processes of Cu-encapsulated nitrates using a decoupled model between heat transfer and mechanical deformation. However, this work did not consider the variation in density of the liquid PCM which cannot be ignored at high pressures [27]. Although the shell thickness of PCM capsules need be adjusted to make a compromise between mechanical stability and heat storage density, little work has been conducted on its effects on the comprehensive heat storage performance.

Therefore, this paper develops a new thermo-mechanical model to evaluate comprehensive heat storage performance of different types of spherical PCM capsules. This model takes into account density variations of the liquid phase PCM and pressure-dependent solid-liquid equilibria together with energy conservation and shell stress during the PCM melting process. On the basis of the model, the melting characteristics of PCM within a capsule are examined, including the evolutions of internal pressure, melting point, latent heat and stored energy as well as melting time frame. Special attention is paid to the effects of shell thickness on the melting characteristics， mechanical stability and energy storage capacity. The model is also applied to predict the minimum shell thickness to avoid cracking at specified PCM bead size and shell materials. This study provides a fundamental understanding of comprehensive energy storage performance of encapsulated PCM and significant references for tailoring shell thickness of encapsulated PCM to achieve optimum, comprehensive energy storage performance.

2. Mathematical Models

115 *2.1. Geometry and main hypotheses*

116 The geometry of a spherical capsule under melting of PCM is shown in Fig. 1,
117 including a shell and liquid/solid PCM. The internal and external radii of the shell are
118 referred to as r_i and r_e, respectively. The position of the melting front is labelled r_m. The radii
119 or position of the melting front, vary during melting of the PCM.

120 The main hypotheses adopted to simplify the model are as follows [26, 27]: (a) specific
121 heat c_{ps} and thermal conductivity λ_s are constant for the solid phase of PCM with non-
122 deformability; (b) specific heat c_{pl} and thermal conductivity λ_l are constant for the liquid
123 phase of PCM; (c) convection heat transfer inside the small-sized capsule is negligible; (d)
124 viscous energy dissipation of the liquid is also negligible; (e) the liquid within the shell has
125 uniform pressure; (f) the shell is considered to be homogeneous, isotropic and exhibiting
126 linear elastic behaviour indicated by Young's modulus, with constant values of density ρ_c,
127 specific heat c_{pc} and thermal conductivity λ_c; (g) the pressure and temperature are known
128 and uniform at the external wall of the shell; (h) there are equalities of pressure and
129 temperature at the PCM/shell interface. The spherical symmetry from the above hypotheses
130 allows reduction of the original three-dimensional problem into a one-dimensional one under
131 a spherical coordinates system (r, θ, φ) for the melting process before shell cracking.

132 *2.2. Heat transfer modelling for spherical capsule*

133 The melting process of PCM is modelled using the enthalpy method based on a fixed
134 grid [29] with directly solving the temperature field. According to the aforementioned main
135 hypotheses (a-e), the energy conservation equation for the capsule can be written as

$$\begin{cases} \dfrac{\partial\left[\left(\rho c_p\right)_{eq} T_i\right]}{\partial t} = \dfrac{1}{r^2}\dfrac{\partial}{\partial r}\left(\lambda_{eq} r^2 \dfrac{\partial T_i}{\partial r}\right) - \dfrac{\partial\left(\rho_{eq}\Delta h_m\right)}{\partial t} & \text{for } 0 \le r \le r_i, \\ \dfrac{\partial\left(\rho_c c_{pc} T_c\right)}{\partial t} = \dfrac{1}{r^2}\dfrac{\partial}{\partial r}\left(\lambda_c r^2 \dfrac{\partial T_c}{\partial r}\right) & \text{for } r_i < r \le r_e, \end{cases} \tag{1}$$

where T_i and T_c represent the temperature distributions in the PCM and shell layers, respectively; Δh_m denotes the melting enthalpy which can be defined as a product of latent heat L_m and local liquid fraction f_l, i.e. $\Delta h_m = f_l L_m = (1 - f_s) L_m$; f_s is local solid fraction; $(\rho c_p)_{eq}$, ρ_{eq} and λ_{eq} denote the equivalent heat capacity, density and thermal conductivity, respectively. They are given by

$$\begin{cases} (\rho c_p)_{eq} = \rho_s c_{ps} f_s + \rho_l c_{pl} (1 - f_s), \\ \rho_{eq} = \rho_s f_s + \rho_l (1 - f_s), \\ \lambda_{eq} = \lambda_s f_s + \lambda_l (1 - f_s). \end{cases} \tag{2}$$

where ρ_s and ρ_l denote the densities of solid and liquid phases of PCM, respectively. The detailed derivation of Eqn. (1) for the PCM region is presented in Appendix A.

For the pure PCM with a fixed melting temperature T_m at a specified pressure, the local solid fraction can be defined as

$$f_s(r,t) = \begin{cases} 0, & T_i \geq T_m \\ 1, & T_i < T_m \end{cases}. \tag{3}$$

Based on the hypotheses (g) and (h), boundary conditions of heat transfer can be expressed as

$$\begin{cases} -\lambda_{eq} \dfrac{\partial T_i}{\partial r} = 0 \ \text{ at } r = 0, \\ \lambda_{eq} \dfrac{\partial T_i}{\partial r} = \lambda_c \dfrac{\partial T_c}{\partial r}, \text{and } T_i = T_c \ \text{ at } r = r_i, \\ T_c = T_e(t) \ \text{ at } r = r_e, \end{cases} \tag{4}$$

where $T_e(t)$ denotes the temperature at the external surface of shell. Initially, $T_i(r,0) = T_c(r,0) = T_0$, which is a specified initial temperature in the simulations. Therefore, $T_e(t) = T_0 + \gamma t$, where γ is the heating rate at the external surface of the shell.

The ratio of melted volume at a time t to the initial volume V_{s0} of solid PCM is denoted by $f^*(t)$, which is referred to as liquid fraction in the following. The liquid fraction can be calculated by

$$f^*(t) = 1 - \frac{3}{r_{i0}^3}\int_0^{r_i} r^2 f_s(r,t)dr. \tag{5}$$

where r_{i0} are the initial values of r_i.

The total energy stored within the PCM bead during melting mainly consists of latent energy and sensible energy, which can be written as

$$ES(f^*) = \int_0^{f^*} \rho_s V_{s0} L_m d\vartheta + \int_0^{V_{s0}} \int_{T(f^*=0)}^{T(f^*)} \left(\rho c_p\right)_{eq} d\vartheta dV. \tag{6}$$

2.3. Thermodynamic equilibrium dependent on pressure

It should be noted that liquid-solid phase equilibrium exists at the melting front, with an equality of Gibbs free energy between liquid and solid phases. The Gibbs free energy can be estimated by a second order Taylor expansion based on fundamental thermodynamic relations, which is expressed as [26]

$$\begin{aligned} g_j(T_m,P) = g_{j0} - s_{j0}(T_m - T_{m0}) + \frac{1}{\rho_{j0}}(P - P_0) - \frac{1}{2}\frac{c_{pj0}}{T_{m0}}(T_m - T_{m0})^2 \\ -\frac{1}{2}\frac{\beta_{j0}}{\rho_{j0}}(P - P_0)^2 + \frac{\alpha_{j0}}{\rho_{j0}}(T_m - T_{m0})(P - P_0), \end{aligned} \tag{7}$$

where the index $j = l$ or s represents liquid or solid phase; T_m is the melting temperature at the pressure P; $g_{j0} = g_j(T_{m0}, P_0)$ denotes the Gibbs free energy at T_{m0} and P_0; T_{m0} is the melting temperature at P_0 denoting reference pressure; s_j represents the specific entropy; α_j denotes the thermal expansion coefficient; β_j denotes the isothermal compressibility; and the subscript 0 refers to (T_{m0}, P_0) conditions. The detailed derivation of Eqn. (7) is presented in Appendix B.

Applying the liquid-solid equilibrium condition ($g_l = g_s$), the melting temperature as a function of pressure is obtained:

$$T_m(P) = T_{m0} + \frac{-j + \sqrt{j^2 - 4ik}}{2i}, \tag{8}$$

with

$$\begin{cases} i = \dfrac{c_{pl0} - c_{ps0}}{2T_{m0}}, \\ j = (s_{l0} - s_{s0}) - \left(\dfrac{\alpha_{l0}}{\rho_{l0}} - \dfrac{\alpha_{s0}}{\rho_{s0}}\right)(P - P_0), \\ k = -\left(\dfrac{1}{\rho_{l0}} - \dfrac{1}{\rho_{s0}}\right)(P - P_0) + \dfrac{1}{2}\left(\dfrac{\beta_{l0}}{\rho_{l0}} - \dfrac{\beta_{s0}}{\rho_{s0}}\right)(P - P_0)^2. \end{cases} \tag{9}$$

The enthalpy difference between the liquid and solid phases (i.e. latent heat L_m) at thermodynamic equilibrium ($g_l = g_s$) can be expressed as [26]

$$L_m(T_m, P) = \Delta s_m(T_m, P) T_m. \tag{10}$$

where $\Delta s_m(T_m, P)$ denotes entropy difference between the liquid and solid phases. According to the Gibbs relation based on Gibbs free energy [30], Eqn. (7) allows writing

$$s_j \equiv -\left.\frac{\partial g_j}{\partial T}\right|_P = s_{j0} + \frac{c_{pj0}}{T_0}(T_m - T_{m0}) - \frac{\alpha_{j0}}{\rho_{i0}}(P - P_0), \tag{11}$$

and therefore

$$\Delta s_m = (s_{l0} - s_{s0}) + \left(\frac{c_{pl0} - c_{ps0}}{T_{m0}}\right)(T_m - T_{m0}) - \left(\frac{\alpha_{l0}}{\rho_{l0}} - \frac{\alpha_{s0}}{\rho_{s0}}\right)(P - P_0). \tag{12}$$

Similarly according to the Gibbs relation based on Gibbs free energy [30], the expression of PCM density can be derived from Eqns. (7) as

$$\frac{1}{\rho_j} \equiv \left.\frac{\partial g_j}{\partial P}\right|_T = \frac{1}{\rho_{j0}}\left[1 + \alpha_{j0}(T_m - T_{m0}) - \beta_{j0}(P - P_0)\right], \tag{13}$$

Some thermodynamic databases usually provide values of these parameters $s_{j0}, \rho_{j0}, c_{pj0}, \alpha_{j0}$ and β_{j0}. The variations of melting temperature, latent heat and density of PCM with pressure are involved in Eqns. (8-10) and (12-13).

2.4. Pressure variation caused by phase change

Considering the spherical symmetry of the studied capsule shell before cracking in a spherical coordinates system (r, θ, φ) and based on the hypothesis (f), the equilibrium equation of elastic mechanics can be simplified as [31]

$$\frac{d\sigma_{rr}}{dr} + \frac{2(\sigma_{rr} - \sigma_{\theta\theta})}{r} = 0, \tag{14}$$

where σ_{rr} and $\sigma_{\theta\theta}$ denote normal stress components of the shell.

From the hypothesis (e), the liquid pressure inside the shell can be represented by P. Based on hypotheses (g) and (h), the boundary conditions for the elastic deformation of the shell are

$$\sigma_{rr}(r = r_{i0}) = -P, \qquad \sigma_{rr}(r = r_{e0}) = 0, \tag{15}$$

where r_{e0} are the initial values of r_e.

The temperature change ΔT that the shell undergoes leads to thermal stress in the shell, which is proportional to the thermal expansion coefficient of the shell material α_c. By combining strain-displacement and stress-strain relations with thermal stress [27], the stress-displacement relations are obtained as

$$\sigma_{rr} = \delta\left(\frac{du}{dr} + \frac{2u}{r}\right) + 2\mu\frac{du}{dr} - \alpha_c\Delta T(3\delta + 2\mu), \tag{16}$$

$$\sigma_{\theta\theta} = \delta\left(\frac{du}{dr} + \frac{2u}{r}\right) + \frac{2\mu u}{r} - \alpha_c\Delta T(3\delta + 2\mu), \tag{17}$$

where u denotes the shell displacement which only has radial component u_r (i.e. $u = u_r$); δ and μ are Lamé's constants calculated with the Young's modulus E_c and Poisson's ratio ν_c as

$$\delta = \frac{E_c\nu_c}{(1 + \nu_c)(1 - 2\nu_c)}, \mu = \frac{E_c}{2(1 + \nu_c)}. \tag{18}$$

By merging Eqns. (16) and (17) into Eqn. (14), the simplified Lamé's equation is derived as

$$\frac{d^2u}{dr^2} + \frac{2}{r}\frac{du}{dr} - \frac{2u}{r^2} = 0. \tag{19}$$

Solving Eqn. (19) with the boundary conditions in Eqn. (15), yields the elastic description of the shell as

$$u(r) = \frac{r_{i0}^3}{r_{e0}^3 - r_{i0}^3}\left(\frac{r_{e0}^3}{4r^2\mu} + \frac{r}{3\delta + 2\mu}\right)P + r\alpha_c\Delta T, \tag{20}$$

$$\sigma_{rr}(r) = \frac{r_{i0}^3}{r_{e0}^3 - r_{i0}^3}\left(-\frac{r_{e0}^3}{r^3} + 1\right)P, \tag{21}$$

$$\sigma_{\theta\theta}(r) = \frac{r_{i0}^3}{r_{e0}^3 - r_{i0}^3}\left(\frac{r_{e0}^3}{2r^3} + 1\right)P. \tag{22}$$

199 The volume displacement for $r = r_{i0}$ is written as

$$\Delta V = \frac{4}{3}\pi\left[\left(r_{i0} + u(r_{i0})\right)^3 - r_{i0}^3\right]. \tag{23}$$

200 During the melting process, the volume expansion of the PCM caused by the density
201 difference between liquid and solid phases at a time t is

$$\Delta V = V_{s0}\left(\frac{\rho_s - \rho_l}{\rho_l}\right)f^*(t). \tag{24}$$

202 From Eqns. (23) and (24), it can be derived that

$$u(r_{i0}) = r_{i0}\left(\sqrt[3]{\frac{\rho_s - \rho_l}{\rho_l}f^*(t) + 1} - 1\right), \tag{25}$$

203 which, combined with Eqn. (20), gives

$$P(t) = \frac{2(r_{e0}^3 - r_{i0}^3)E_c\left(\sqrt[3]{(\rho_s - \rho_l)f^*/\rho_l + 1} - (1 + \alpha_c\Delta T)\right)}{r_{i0}^3(2 - 4\nu_c) + r_{e0}^3(1 + \nu_c)}. \tag{26}$$

204 *2.5. Equivalent critical pressure of cracking*

205 The equivalent critical internal pressure as the shell cracking limit is calculated with the
206 von Mises criterion. By virtue of the spherical symmetry, the von Mises stress in the shell
207 reduces to [31]

$$\sigma_v = \sigma_{\theta\theta} - \sigma_{rr}, \tag{27}$$

208 which has the maximum value at $r = r_{i0}$. When the maximum von Mises stress reaches the
209 tensile strength of the shell material σ_t, the shell will crack and loose the encapsulated PCM

[20, 22]. According to this situation, the equivalent critical pressure of cracking can be derived as

$$P_{eq} = \frac{2}{3}\left(1 - \frac{r_{i0}^3}{r_{e0}^3}\right)\sigma_t \tag{28}$$

2.6. Solving procedure

In the proposed model, the melting process of PCMs is coupled with the internal pressure change via variation of the volume inside the shell, melting point, latent heat and liquid density. The above equations thus need iterations to obtain the melting dynamic characteristics, mechanical behaviour and heat storage performance. The flowchart of the solving procedure for the proposed model is illustrated in Fig. 2. The flowchart also includes the input and output parameters. In each time step, Δt, the solving procedure needs to repeatedly undergo internal iterations until satisfying convergence criteria, and then the calculated instantaneous results are output for analysis. The relaxation factor, φ, is used to speed up the convergence. If the melting process is not completed (i.e. $f^*(t) < 1$), the solving procedure turns into the next time step. When $f^*(t) = 1$, the solving procedure is over and the resulting internal pressure is used to examine the mechanical behaviour of the shell combined with the equivalent critical pressure of cracking calculated by Eqn. (28).

3. Validation of the model

In order to validate the proposed model, the results calculated based on the model established in this paper were compared with those in literature for the melting process of salt particles coated in a graphite matrix [26] and a SiC shell [27] with the same properties and hypotheses. The heat conduction in the matrix or shell is not included for the two types of salt capsules. The properties of salts and SiC used in the model validation are listed in Table 1 and Table 2, respectively. The graphite matrix was modelled as a thick shell with a non-

moving external wall [26]. The property of the graphite matrix required in the model validation is the rigidity modulus, which is 8 GPa. The input parameters are the same for the simulations of the melting process of the two types of salt capsules, which are listed in Table 3. The radius of salt beads and the thickness of the graphite or SiC shell are set to 1 mm and 200 μm, respectively. The Fig. 3(a) shows the comparison between the current study and the literature [26] in the variations of solid fraction and internal pressure during melting of a single salt bead. The relative errors in the solid fraction and internal pressure are shown in Fig. 3(b). It can be found that the maximum relative errors are both less than 8%. Fig. 3(c) displays the comparison between the current study and the literature [27] in the variations of melting temperature and latent heat during melting of a single salt bead. The relative errors in the melting temperature and latent heat are depicted in Fig. 3(d). We can see that the maximum relative errors are both less than 6%. Except for tiny discrepancies in values, the results in all aspects obtained in this study agree satisfactorily with the literature [26, 27], indicating that the heat transfer model in Section 2.2 and the pressure-dependent thermodynamic equilibrium model in Section 2.3 together with the pressure variation model in Section 2.4 are sufficiently accurate. The established model can therefore be used to analyse the thermo-mechanical behaviour and evaluate heat energy storage performance of PCM capsules.

4. Results and discussions

$NaNO_3$-KNO_3 eutectic salts [26, 27] and Cu [21, 24], as typical high temperature PCMs applicable to different temperature regions, have attracted much attention. Based on the melting point, corrosion inhibition, mechanical strength and thermal conductivity, SiC and Ni are potential encapsulating materials for salts and Cu, respectively. In this study the SiC-encapsulated salt and Ni-encapsulated Cu are selected as an illustration to demonstrate heat

transfer and mechanical behaviour of encapsulated PCMs during melting using the validated models. The adopted approach and resulting characteristics could be extended to other types of encapsulated PCMs. The thermodynamic properties of salts and Cu as PCMs at atmospheric pressure P_0 are listed in Table 1. The properties of SiC and Ni as shell materials are listed in Table 2. It should be noted that the actual properties of the shell depend on actual fabricated effect. The radius of the solid PCM bead is prescribed as 1 mm. The temperature at the external surface of the shell is specified as increasing from 220˚C for the salt capsule and 1080˚C for the Cu capsule at a heating rate of 5˚C/min until the PCMs are totally melted in the simulations. The time step is set to 0.1 s. These input parameters are summarized in Table 3.

4.1 Effects of shell thicknesses on thermo-mechanical behaviour of salt capsules

Fig. 4(a) illustrates the evolution of internal pressure under different shell thicknesses during the melting process of salts ($f^*: 0 \rightarrow 1$). The main finding is that the increasing rate of internal pressure decreases with the decrease in shell thickness. As a consequence of PCM volume expansion during the melting process, the internal pressure will progressively increase and the shell will strain due to the increasing pressure. The pressure is no longer subject to linear with respect to the liquid fraction and the calculated maximum internal pressure will not reach an incredible value of over 3000 MPa, which is different from cases investigated without considering density change dependent on pressure in the work of Pitié *et al*. [27]. Fig. 4(b) compares the equivalent critical pressure as the cracking limit of SiC to the calculated maximum internal pressure in the SiC shell for different shell thicknesses. The maximum internal pressure and equivalent pressure both decrease with the decrease in shell thickness, while the latter has a larger decreasing rate. An intersection point between the maximum internal pressure and equivalent pressure appears at shell thickness $a = 67$ μm. It indicates that the shell can avoid cracking during the melting process of salts for $a \geq 67$ μm,

whereas the shell will crack at some melting stage for $a < 67$ μm. The cracking point is marked according to the equivalent pressure of cracking limit represented by the horizontal line for $a = 50$ μm as shown in Fig. 4(a). The corresponding liquid fraction at the cracking point is 0.53. Through calculation according to Eqn. (28) and the calculated maximum internal pressure for $a = 50$ μm, we can infer that if the tensile strength of SiC could be augmented over 2.26 GPa the shell with $a = 50$ μm can also avoid cracking. According to Eqns. (26) and (28), the maximum internal pressure and equivalent critical pressure both depend on the ratio of core radius to shell thickness r_{i0}/a. Therefore, the condition of avoiding cracking for different size SiC-shell/salts-core capsules can be deduced by the critical shell thickness of 67 μm for the salt bead of a 1 mm radius, which is $r_{i0}/a \leq 14.9$.

According to Eqn. (13), the density of the liquid PCM is dependent on the pressure. Although the isothermal compressibility of the liquid PCM is very small, the density variation cannot be ignored at high pressures. Fig. 5(a) elucidates the evolution of the density of liquid salts as a function of liquid fraction. Under the action of increasing internal pressures as shown in Fig. 4(a), the density of liquid salts gradually increases with the liquid fraction and its difference with that of solid salts gradually diminishes. Therefore, the volume expansion rate caused by phase change will be decreased, which slows down the pressure change at high pressures as shown in Fig. 4(a). The melting temperatures of coated salts at different melting stages under different shell thicknesses are shown in Fig. 5(b). It can be found that the melting temperature visibly increases as the melting process carries on. The coated salts must be heated up to at least 510.9 K, which is 14.8 K higher than the melting temperature at atmospheric pressure, to achieve complete melting for $a = 200$ μm. According to Eqns. (8) and (9), it is evident that the melting temperature mainly depends on the internal pressure. Thus variations of the melting temperature with the liquid fraction and shell thickness show the trends similar to the internal pressure. Fig. 5(c) shows the variation of

latent heat of salts during the melting process under different shell thicknesses. As both the internal pressure and melting point rise, the latent heat remarkably decreases. For $a = 200$ μm, the latent heat reduces from 105 kJ/kg to 87.2 kJ/kg. This results in the effect of a loss in stored heat energy by absorption of latent heat. The decrease of shell thickness minimises the decrease of latent heat during the melting process and thus can increase the storage capability.

Due to the progressive increase of melting temperature, the wall temperature of the capsule should be increased continuously to trigger ongoing melting. Fig. 6(a) depicts the required wall temperature corresponding to different melting stages under different shell thicknesses of salt capsules at a heating rate of 5˚C/min. The required maximum wall temperature for completely melting is 513.3 K at $a = 200$ μm. The required maximum wall temperature is reduced with the decrease in shell thickness. Fig. 6(b) displays the heat transfer rate at the salt capsule wall during the melting process under different shell thicknesses. The heat transfer rate has little change with the decrease in shell thickness for liquid fraction $f^* \leq 0.1$, while it increases with the decrease in shell thickness for $f^* > 0.1$. This is attributed to the smaller decrease of latent heat for a thinner shell as shown in Fig. 5(c).

4.2 Effect of shell thickness on heat storage performance of salt capsules

Fig. 7(a) demonstrates the melting time of coated salts under different shell thicknesses. The melting rate in the early stage of the melting process is less than that in the late stage for various shell thicknesses. This is due to the slow change of melting temperature in the early stage and its abrupt increase in the late stage. The shell thickness has no effect on the start time of the melting process, while the decrease in shell thickness speeds up the melting process and thus brings forward the end time of melting. This is consistent with the lower melting temperature for thinner shell thickness. The shortened melting period will be a benefit to the charging efficiency of heat energy.

The energy stored in the salt beads during the melting process is also examined for capsules with different shell thickness as shown in Fig. 7(b). The stored latent energy increases linearly with the liquid fraction, while the stored sensible energy sharply increases in the early stage of the melting process and slightly increases in the late stage. The change trends of the stored sensible energy are determined by the changes in melting temperature and wall temperature. In the early stage of the melting process, the stored sensible energy and latent energy represent a similar share of the total energy. In the late stage of melting, the stored latent energy is larger than the stored sensible energy. From this figure, we can also find that the capsule with a thicker shell stores larger sensible energy, while the capsule with a thinner shell stores larger latent heat during the melting process. The difference in the stored sensible energy for different shell thicknesses progressively decreases during the melting process, whilst the reverse is observed for the stored latent energy. The curves of stored total energy as shown in Fig. 7(b) show that the salt bead coated by a thinner shell offers better energy storage capacity.

The shell can also store some sensible heat during the salt melting process. As shown in Table 4, the thermal energy storage density, including the sensible heat stored in the shell, is compared for salt capsules with different shell thickness. Both the mass-based and volume-based energy storage densities notably increase with a decrease in the shell thickness. They increase by about 35.4 kJ/kg (55.1%) and 63.5 MJ/m^3 (37.6%), respectively, as the shell thickness reduces from 200 μm to 50 μm. The calculations indicate that the different sized capsules have the same energy storage density when they have the same r_{i0}/a value. The results imply that enhancing the tensile strength of shell materials to enable the thinner shell for encapsulated salts has great promise in further promotion of thermal energy storage density.

4.3 Comparative analysis between salt and Cu capsules

Further simulations indicate that the effects of shell thickness of the Ni-shell/Cu-core capsule on the comprehensive energy storage performances are similar to those of the SiC-shell/salts-core capsule. However, due to the differences in the thermophysical and mechanical properties, the maximum internal pressure and equivalent critical pressure are notably different between the two types of capsules. Fig. 8(a) compares the equivalent critical pressure as the cracking limit of Ni to the calculated maximum internal pressure in the Ni shell for different shell thicknesses. This figure indicates that the Ni shell can accommodate the volume expansion of copper bead as the shell thickness is 400 μm, which coincides with the experimental result of Zhang *et al*. [24]. From the intersection point between the maximum internal pressure and equivalent critical pressure, it can be inferred that the critical shell thickness for the Cu capsule is 248 μm for the Cu bead of 1 mm in radius. Similarly, it can also be derived that the condition for avoiding cracking for different sized Ni-shell/Cu-core capsules is $r_{i0}/a \leq 4.0$. By comparing Fig. 8(a) with Fig. 4(b), it is found that the maximum internal pressure in the Cu capsule is much higher than that in the salt capsule at the same shell thickness. This can be easily explained, based on Eqn. (26), by the discrepancy between the two types of PCMs in the relative density difference $(\rho_s - \rho_l)/\rho_l$, as shown in Fig. 8(b). From this figure, it can be seen that the relative density difference of Cu is larger than that of salts at the same shell thickness of 200 μm during the whole melting process. The larger relative density difference results in a higher internal pressure. Meanwhile, it can be found that the equivalent critical pressure of the Cu capsule is much less than that of the salt capsule by comparing Fig. 8(a) with Fig. 4(b). This is because the Ni as the shell of Cu capsule has smaller tensile strength than SiC as listed in Table 2. Therefore, a larger relative density difference and a smaller tensile strength lead to a smaller critical r_{i0}/a for avoiding cracking of the Cu capsule in comparison with the salt capsule.

382 The above results indicate that the capsules have optimum comprehensive energy
383 storage performance when they possess the critical shell thickness. Fig. 9 displays the
384 comparison between the salts and Cu capsules with the respective critical shell thickness in
385 the melting point increment during the melting process and the melting time. As shown in Fig.
386 9(a), the melting point increment of Cu is higher than that of salts in the early stage of
387 melting, while the increment of Cu is lower in the late stage. This feature is determined by
388 the thermodynamic properties and internal pressure according to the Eqns. (8) and (9).
389 Although the maximum internal pressure in the Cu capsule is higher than that in the salt
390 capsule, the eventual melting point increment of Cu is lower. This is different from the
391 change tendency that the melting point increases with the internal pressure. The discrepancy
392 indicates that the thermodynamic properties of PCMs play a critical role in the variation of
393 melting point. Corresponding to the melting point increment, the Cu capsule exhibits slower
394 melting rate in the early stage and faster melting rate at the late stage than the salt capsule for
395 an equal sized PCM bead, as shown in Fig. 9(b). Further, it can be found in Fig. 9(b) that the
396 melting period of a Cu bead is about 54 seconds lower than that of a salt bead at the same
397 radius of 1 mm.
398
399 **5. Conclusions**
400 A thermo-mechanical model allowing for liquid PCM density variation at high
401 pressures was set up to elaborate the behavior of a spherical capsule during melting of PCM
402 for HTTES. The melting dynamic characteristics of PCM are notably different from those
403 without considering the liquid density variation in the work of Pitié *et al*. [27]. The internal
404 pressure is no longer increasing linearly with the increase of liquid fraction and the increasing
405 rate gradually reduces. Hence the internal pressure does not increase to an incredibly high

406 value during the melting process. Accordingly, the changing rates of the melting point and
407 latent heat of PCM during the melting process progressively decrease until nearly zero.

408 On the basis of the developed model, the effects of shell thickness on the
409 comprehensive energy storage performances of a PCM capsule have been explored. When
410 the size of PCM core is fixed, the decrease of shell thickness reduces the internal pressure
411 increment, and thus diminishes the varying ranges of melting point and latent heat, which
412 results in a diminution of melting period and an augmentation of stored latent energy in the
413 capsule. Therefore increasing the ratio of core radius to shell thickness is beneficial for
414 promoting the energy charging rate and energy storage capacity. However, there exists a
415 maximum ratio of core radius to shell thickness to avoid shell cracking, which is 14.9 and 4.0
416 for SiC-shell/salts-core and Ni-shell/Cu-core capsules, respectively. The maximum ratio of
417 core radius to shell thickness can be elevated by enhancing the tensile strength of shell
418 materials and/or selecting PCMs with small relative density difference between solid and
419 liquid phases. In addition, the thermodynamic properties should be carefully considered in the
420 selection of PCMs, which leads to different melting point increments and melting periods.
421 This is confirmed by the fact that Cu capsules exhibit smaller melting point increment and
422 shorter melting period than salt capsules for the same core radius with their respective critical
423 shell thicknesses. Provided that the properties of PCMs and shell materials meet the main
424 hypotheses described in Section 2.1, and that the PCMs have a fixed melting temperature at a
425 specified pressure, the model can be applied to selection of materials and shell thickness to
426 achieve excellent mechanical stability, fast energy charging rate and high energy storage
427 capacity simultaneously for different types of encapsulated PCMs in HTTES applications.

428

429 **Acknowledgement**

The authors would like to acknowledge the financial support of the Engineering and Physical Sciences Research Council (EPSRC) of the United Kingdom (Grant Nos. EP/N000714/1 and EP/N021142/1), National Natural Science Foundation of China (Grant No. 51606135) and Natural Science Foundation of Hubei Province (Grant No. 2016CFB156).

References

[1] Seitz M, Johnson M, Hübner S. Economic impact of latent heat thermal energy storage systems within direct steam generating solar thermal power plants with parabolic troughs. Energy Conversion and Management. 2017;143: 286-94.

[2] Liu M, Steven Tay NH, Bell S, Belusko M, Jacob R, Will G, et al. Review on concentrating solar power plants and new developments in high temperature thermal energy storage technologies. Renewable and Sustainable Energy Reviews. 2016;53: 1411-32.

[3] Miró L, Gasia J, Cabeza LF. Thermal energy storage (TES) for industrial waste heat (IWH) recovery: A review. Applied Energy. 2016;179: 284-301.

[4] Peng H, Yang Y, Li R, Ling X. Thermodynamic analysis of an improved adiabatic compressed air energy storage system. Applied Energy. 2016;183: 1361-73.

[5] Guo H, Xu Y, Chen H, Zhou X. Thermodynamic characteristics of a novel supercritical compressed air energy storage system. Energy Conversion and Management. 2016;115: 167-77.

[6] Sciacovelli A, Li Y, Chen H, Wu Y, Wang J, Garvey S, et al. Dynamic simulation of Adiabatic Compressed Air Energy Storage (A-CAES) plant with integrated thermal storage – Link between components performance and plant performance. Applied Energy. 2017;185, Part 1: 16-28.

[7] Guizzi GL, Manno M, Tolomei LM, Vitali RM. Thermodynamic analysis of a liquid air energy storage system. Energy. 2015;93: 1639-47.

[8] Sciacovelli A, Vecchi A, Ding YL. Liquid air energy storage (LAES) with packed bed cold thermal storage – From component to system level performance through dynamic modelling. Applied Energy. 2017;190: 84-98.

[9] Tiari S, Qiu S, Mahdavi M. Discharging process of a finned heat pipe–assisted thermal energy storage system with high temperature phase change material. Energy Conversion and Management. 2016;118: 426-37.

[10] Regin AF, Solanki SC, Saini JS. Heat transfer characteristics of thermal energy storage system using PCM capsules: A review. Renewable and Sustainable Energy Reviews. 2008;12: 2438-58.

460 [11] Peng H, Dong H, Ling X. Thermal investigation of PCM-based high temperature thermal energy
461 storage in packed bed. Energy Conversion and Management. 2014;81: 420-7.
462 [12] Karthikeyan S, Ravikumar Solomon G, Kumaresan V, Velraj R. Parametric studies on packed
463 bed storage unit filled with PCM encapsulated spherical containers for low temperature solar air
464 heating applications. Energy Conversion and Management. 2014;78: 74-80.
465 [13] Izquierdo-Barrientos MA, Sobrino C, Almendros-Ibáñez JA. Thermal energy storage in a
466 fluidized bed of PCM. Chemical Engineering Journal. 2013;230: 573-83.
467 [14] Izquierdo-Barrientos MA, Sobrino C, Almendros-Ibáñez JA. Experimental heat transfer
468 coefficients between a surface and fixed and fluidized beds with PCM. Applied Thermal Engineering.
469 2015;78: 373-9.
470 [15] Wu M, Xu C, He Y-L. Dynamic thermal performance analysis of a molten-salt packed-bed
471 thermal energy storage system using PCM capsules. Applied Energy. 2014;121: 184-95.
472 [16] Blaney JJ, Neti S, Misiolek WZ, Oztekin A. Containment capsule stresses for encapsulated phase
473 change materials. Applied Thermal Engineering. 2013;50: 555-61.
474 [17] Elmozughi AF, Solomon L, Oztekin A, Neti S. Encapsulated phase change material for high
475 temperature thermal energy storage – Heat transfer analysis. International Journal of Heat and Mass
476 Transfer. 2014;78: 1135-44.
477 [18] Izquierdo-Barrientos MA, Sobrino C, Almendros-Ibáñez JA. Energy storage with PCM in
478 fluidized beds: Modeling and experiments. Chemical Engineering Journal. 2015;264: 497-505.
479 [19] Pitié F, Zhao CY, Baeyens J, Degrève J, Zhang HL. Circulating fluidized bed heat
480 recovery/storage and its potential to use coated phase-change-material (PCM) particles. Applied
481 Energy. 2013;109: 505-13.
482 [20] Maruoka N, Akiyama T. Thermal stress analysis of PCM encapsulation for heat recovery of high
483 temperature waste heat. Journal of Chemical Engineering of Japan. 2003;36: 794-8.
484 [21] Ma B, Li J, Xu Z, Peng Z. Fe-shell/Cu-core encapsulated metallic phase change materials
485 prepared by aerodynamic levitation method. Applied Energy. 2014;132: 568-74.

[22] Nomura T, Zhu C, Sheng N, Saito G, Akiyama T. Microencapsulation of metal-based phase change material for high-temperature thermal energy storage. Scientific Reports. 2015;5: 9117.

[23] Mathur A, Kasetty R, Oxley J, Mendez J, Nithyanandam K. Using encapsulated phase change salts for concentrated solar power plant. Energy Procedia. 2014;49: 908-15.

[24] Zhang G, Li J, Chen Y, Xiang H, Ma B, Xu Z, et al. Encapsulation of copper-based phase change materials for high temperature thermal energy storage. Solar Energy Materials and Solar Cells. 2014;128: 131-7.

[25] Zhao W, Neti S, Oztekin A. Heat transfer analysis of encapsulated phase change materials. Applied Thermal Engineering. 2013;50: 143-51.

[26] Lopez J, Caceres G, Palomo Del Barrio E, Jomaa W. Confined melting in deformable porous media: A first attempt to explain the graphite/salt composites behaviour. International Journal of Heat and Mass Transfer. 2010;53: 1195-207.

[27] Pitié F, Zhao CY, Caceres G. Thermo-mechanical analysis of ceramic encapsulated phase-change-material (PCM) particles. Energy & Environmental Science. 2011;4: 2117-24.

[28] Parrado C, Cáceres G, Bize F, Bubnovich V, Baeyens J, Degrève J, et al. Thermo-mechanical analysis of copper-encapsulated $NaNO_3$–KNO_3. Chemical Engineering Research and Design. 2015;93: 224-31.

[29] Voller VR, Cross M, Markatos NC. An enthalpy method for convection/diffusion phase change. International Journal for Numerical Methods in Engineering. 1987;24: 271-84.

[30] Yunus AC, Michael AB. Thermodynamics: An engineering approach. New York: McGraw-Hill; 2006.

[31] Chakrabarty J. Theory of Plasticity. 3rd ed. Oxford: Butterworth-Heinemann; 2006.

[32] Janz GJ. Molten salts handbook. New York: Academic Press; 1967.

[33] Giordanengo B, Benazzi N, Vinckel J, Gasser JG, Roubi L. Thermal conductivity of liquid metals and metallic alloys. Journal of Non-Crystalline Solids. 1999;250: 377-83.

[34] Chekhovskoi VY, Tarasov VD, Gusev YV. Calorific properties of liquid copper. High Temperature. 2000;38: 394-9.

513 [35] Kangarlou H, Abdollahi A. Thermodynamic properties of copper in a wide range of pressure and
514 temperature within the quasi-harmonic approximation. International Journal of Thermophysics.
515 2014;35: 1501-11.
516 [36] Dandekar DP, Bartkowski PT. Tensile strengths of silicon carbide (SiC) under shock loading.
517 Aberdeen: Weapons and Materials Research Directorate, Army Research Laboratory; 2001 Mar.
518 Report No.: ARL-TR-2430.
519 [37] Nickel -properties, fabrication and applications of commercially pure nickel. http://www.nickel-
520 alloys.net/commercially_pure_nickel.html.

521

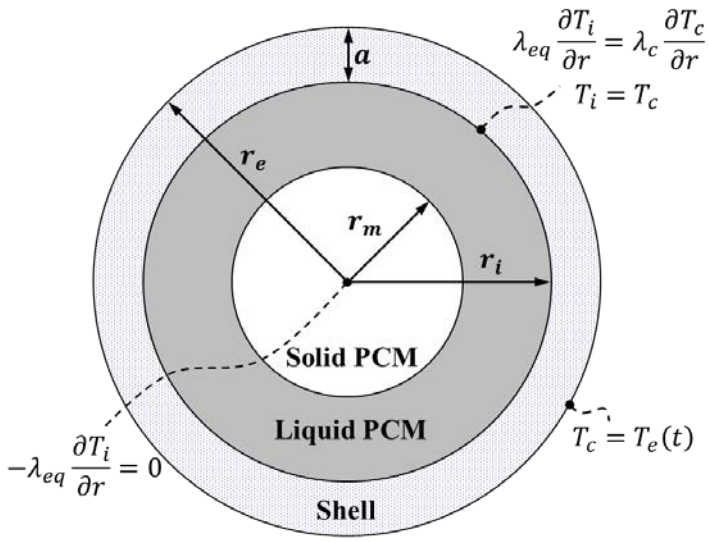

Fig. 1. Geometry of the spherical PCM capsule with boundary conditions.

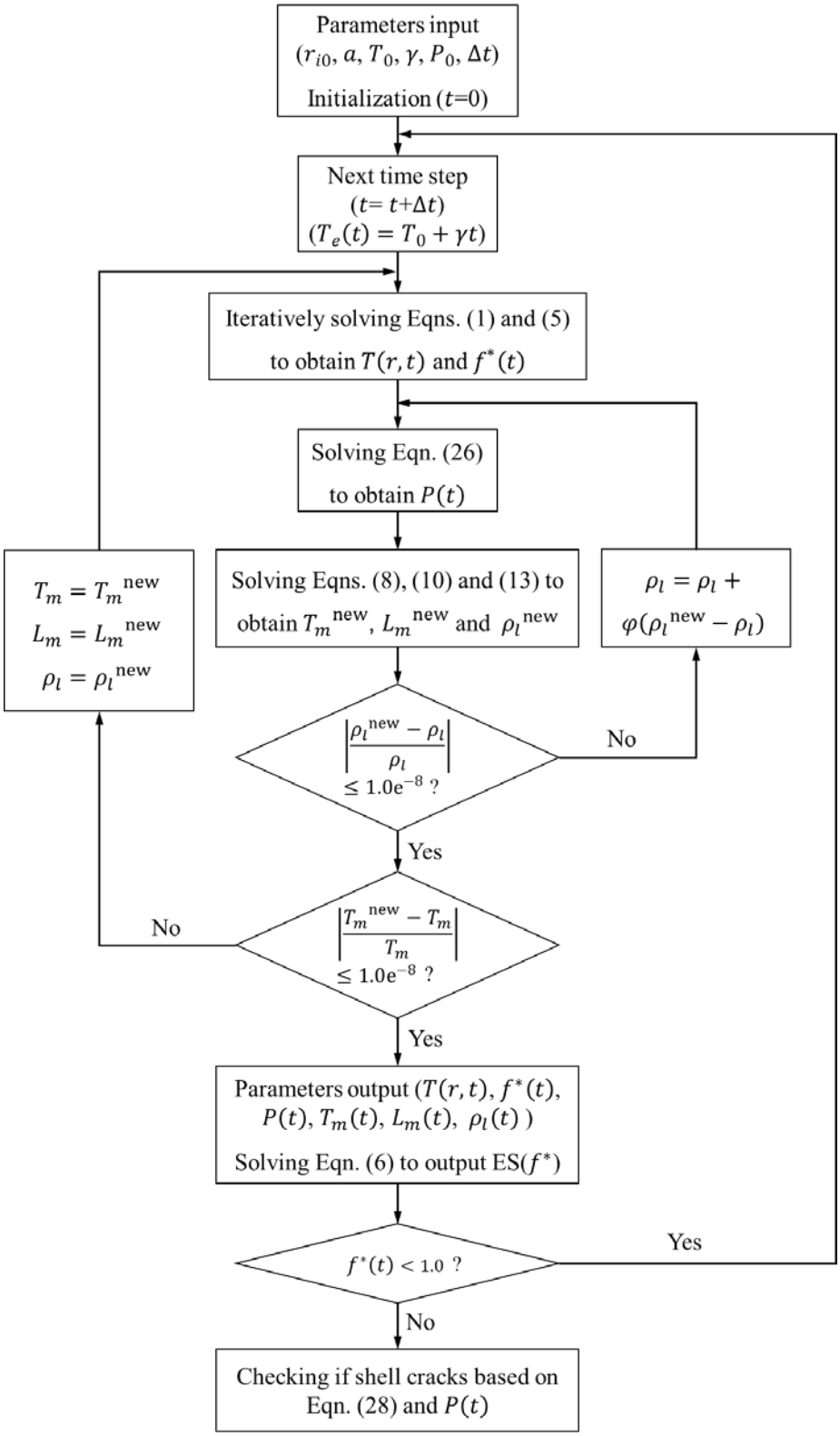

Fig. 2. Flowchart of solving procedure for the proposed model.

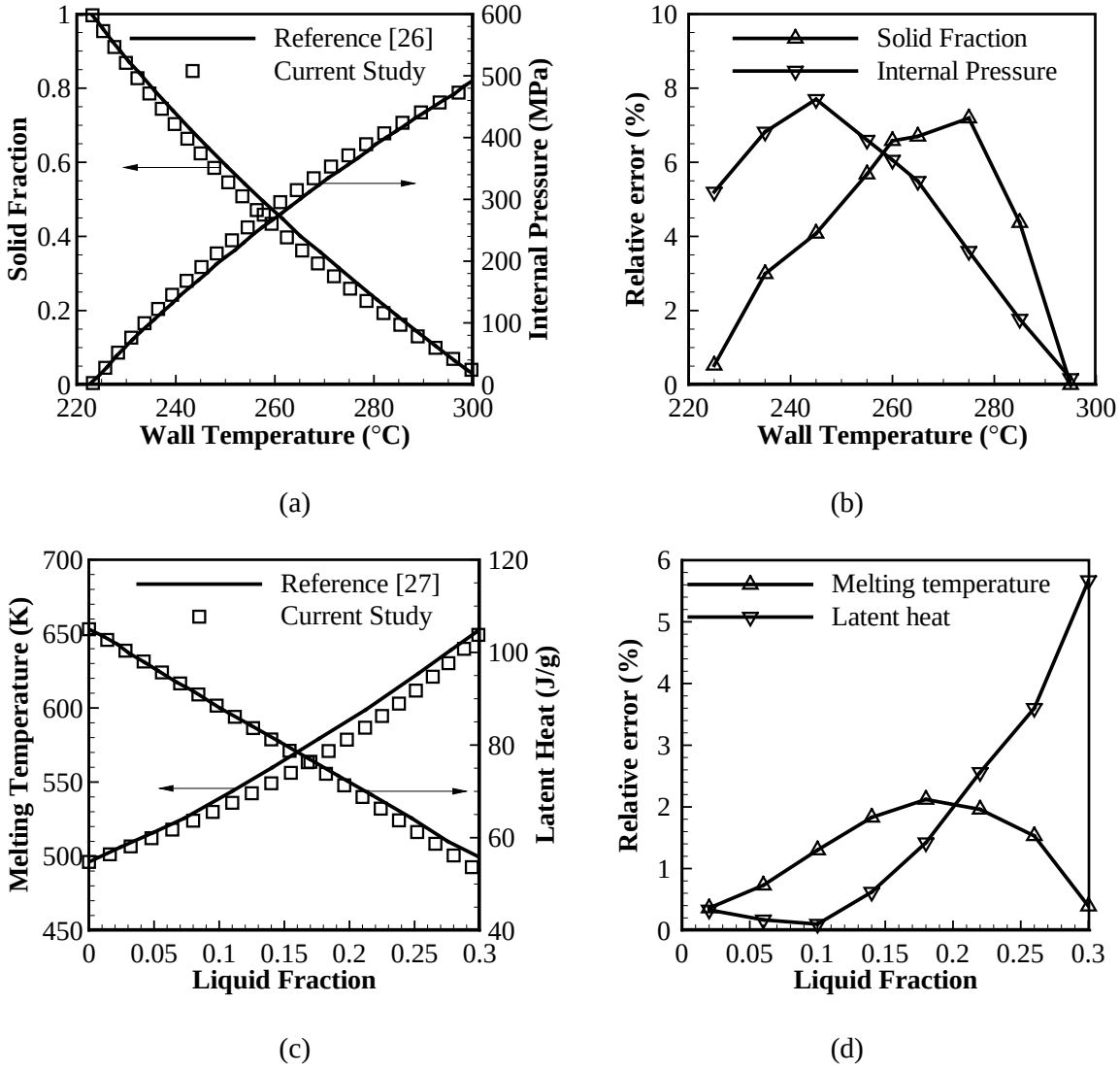

Fig. 3. Comparison with references: (a) Evolution of solid fraction and internal pressure with wall temperature; (b) Relative errors calculated from (a); (c) Evolution of melting temperature and latent heat with liquid fraction; (d) Relative errors calculated from (c).

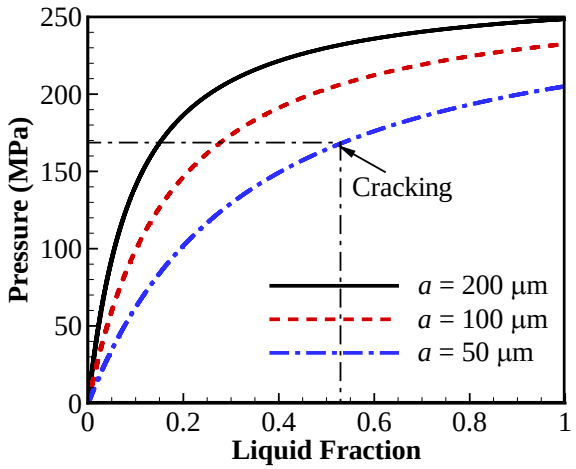

(a)

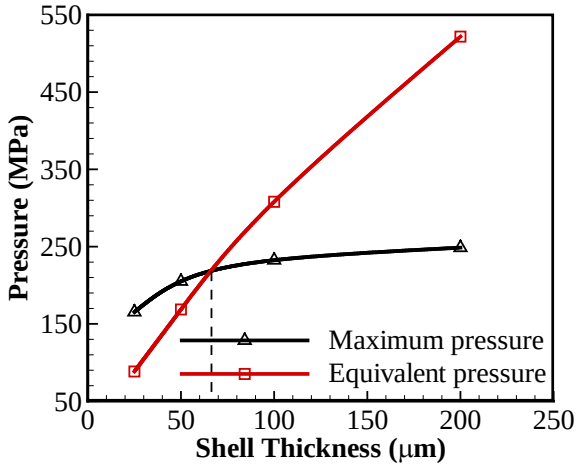

(b)

Fig. 4. Internal pressures under different shell thicknesses of salts capsule: (a) Evolution of pressures during melting; (b) Comparison between the calculated maximum internal pressures and pressures equivalent to the von Mises criterion strength of SiC as the cracking limit of materials. Critical position of cracking is labelled in (a).

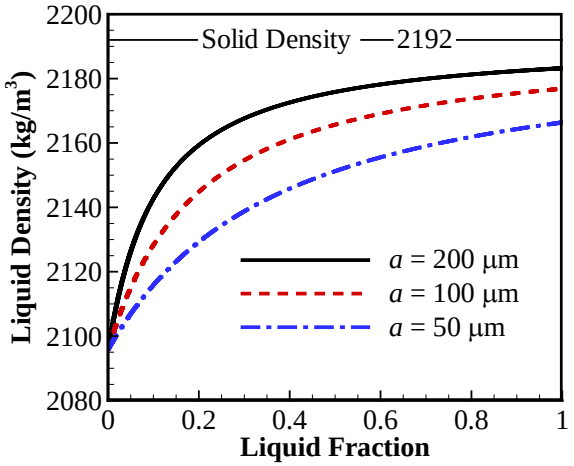

(a)

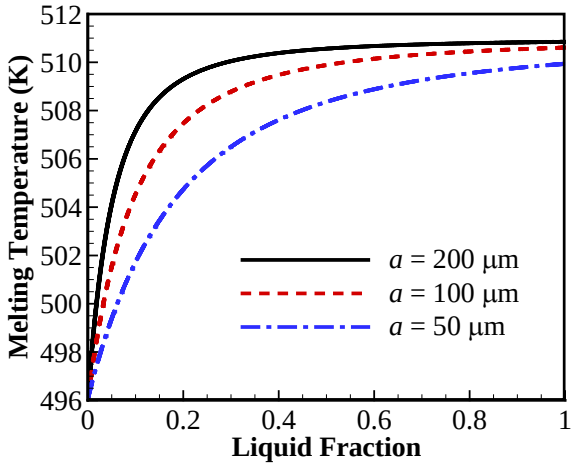

(b)

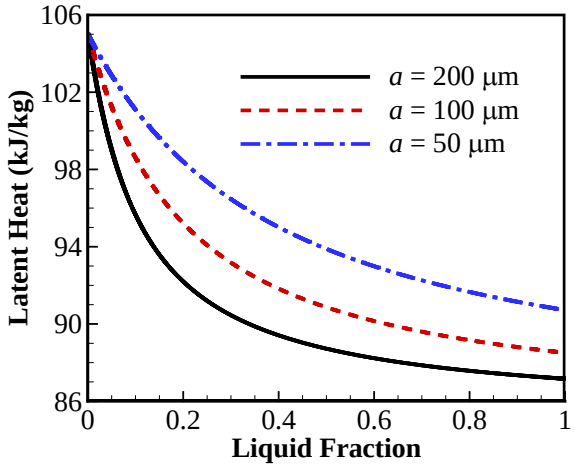

(c)

Fig. 5. Effects of shell thickness on the thermos-physical properties of salts during melting: (a) Evolution of liquid density; (b) Evolution of melting temperature; (c) Evolution of latent heat.

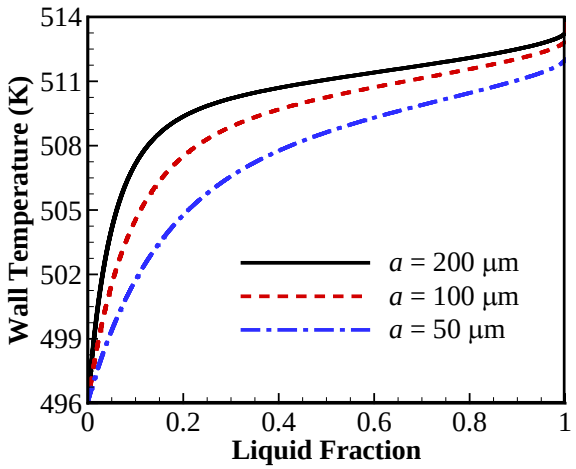

(a)

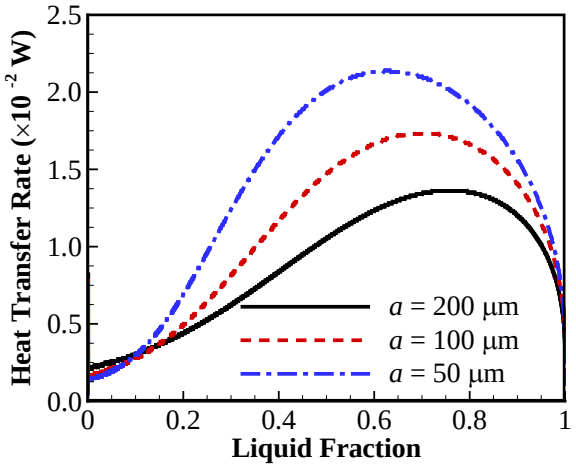

(b)

Fig. 6. Evolutions of wall temperature (a) and heat transfer rate (b) during melting under different shell thicknesses of salts capsule.

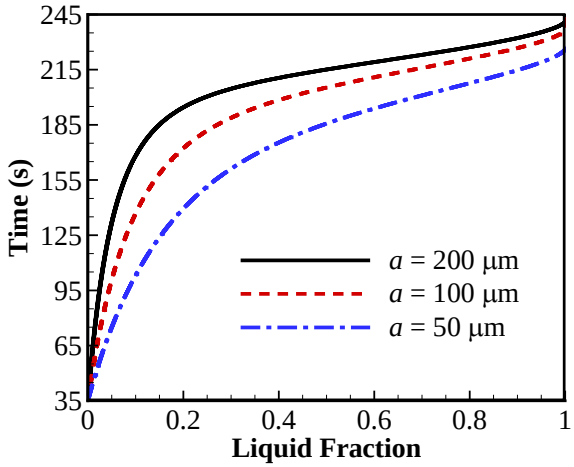

(a)

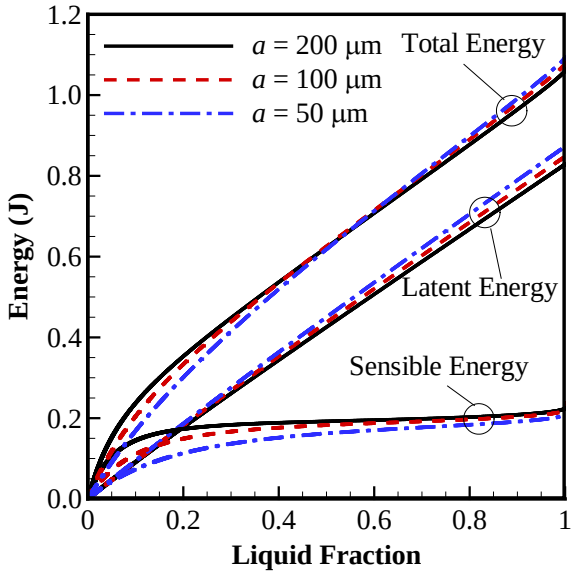

(b)

Fig. 7. Effects of shell thickness of salts capsule: (a) Melting time; (b) Evolution of stored energy.

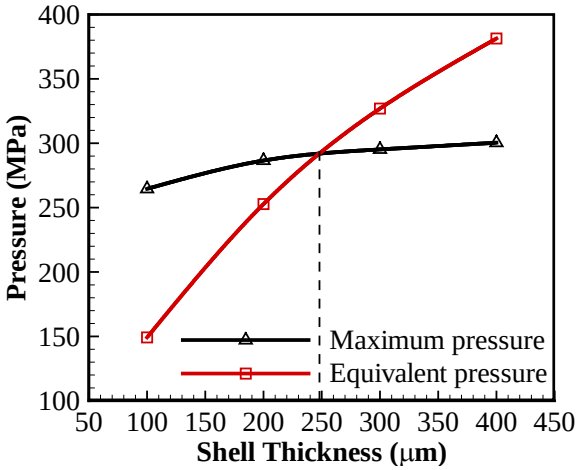

(a)

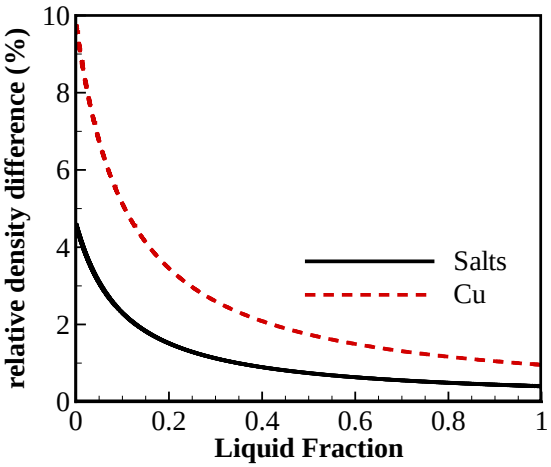

(b)

Fig. 8. (a) Comparison between the calculated maximum internal pressures and pressures equivalent to the von Mises criterion strength of Ni as the cracking limit of materials under different shell thicknesses of Cu capsule; (b) Comparison of relative density difference of solid and liquid phases between salts and Cu at a same shell thickness of 200 μm.

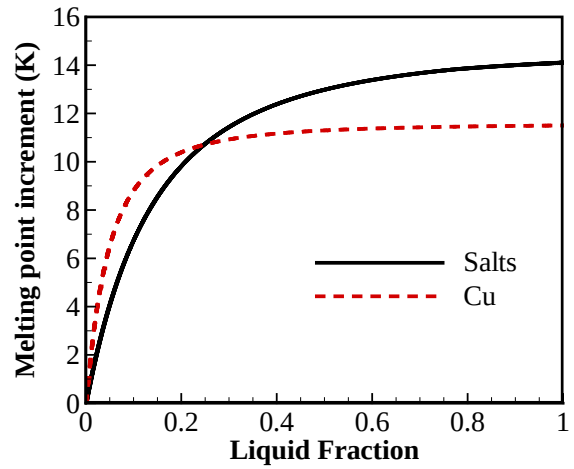

(a)

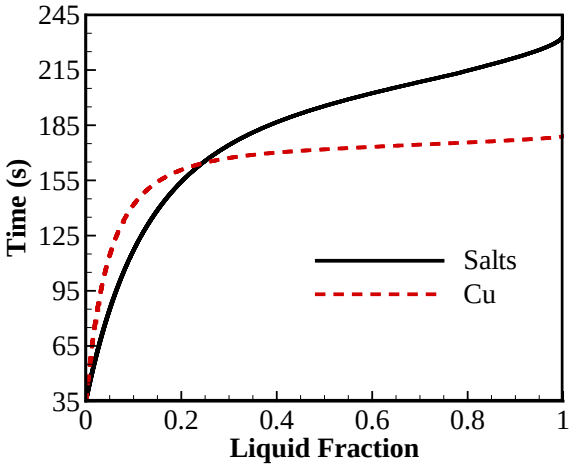

(b)

Fig. 9. Comparison of melting dynamics between salts and Cu capsules with the respective critical shell thickness: (a) Melting point increment; (b) Melting time.

Table 1 Properties of salts [26, 32] and Cu [33-35] used in simulations.

	Properties	Symbol	Salts	Cu	Unit
Liquid state	Density	ρ_{l0}	2096	8020	$kg \cdot m^{-3}$
	Specific heat	c_{pl}	1500	643	$J \cdot kg^{-1} \cdot K^{-1}$
	Compressibility	β_l	1.86×10^{-10}	3.00×10^{-10}	Pa^{-1}
	Thermal expansion	α_l	3.7×10^{-4}	1.05×10^{-4}	K^{-1}
	Thermal conductivity	λ_l	0.8	166	$W \cdot m^{-1} \cdot K^{-1}$
Solid state	Density	ρ_{s0}	2192	8800	$kg \cdot m^{-3}$
	Specific heat	c_{ps}	1430	477	$J \cdot kg^{-1} \cdot K^{-1}$
	Compressibility	β_s	0	0	Pa^{-1}
	Thermal expansion	α_s	0	0	K^{-1}
	Thermal conductivity	λ_s	1	394	$W \cdot m^{-1} \cdot K^{-1}$
L↔S	Melting temperature at P_0	T_{f0}	223	1083	˚C
	Latent heat at (T_{f0}, P_0)	L_{f0}	105	207	$kJ \cdot kg^{-1}$

Table 2 Properties of SiC [36] and Ni [37] in simulations.

Properties	Symbol	SiC	Ni	Unit
Density	ρ_c	3227	8890	$kg \cdot m^{-3}$
Specific heat	c_{pc}	950	456	$J \cdot kg^{-1} \cdot K^{-1}$
Thermal expansion	α_c	4×10^{-6}	1.34×10^{-5}	K^{-1}
Thermal conductivity	λ_c	120	80	$W \cdot m^{-1} \cdot K^{-1}$
Young's modulus	E_c	454	200	GPa
Poisson's ratio	ν_c	0.164	0.31	--
Tensile strength	σ_t	1858	900	MPa

Table 3 Input parameters used in simulations.

Parameters	Symbol	Salts capsule	Cu capsule	Unit
Radius of solid PCM bead	r_{i0}	1	1	mm
Shell thickness	a	25~200	100~400	μm
Initial temperature	T_0	220	1080	˚C
Heating rate of external surface	γ	5	5	˚C·min^{-1}
Initial pressure	P_0	1.01×10^5	1.01×10^5	Pa
Time step	Δt	0.1	0.1	s

Table 4 Thermal energy storage density of a single capsule containing a salts bead with a radius of 1 mm.

Shell thickness (μm)	Mass-based energy storage density (kJ/kg)	Volume-based energy storage density (MJ/m^3)
200	64.2	168.8
100	84.2	206.3
50	99.6	232.3

Appendix

A. Derivation of Eqn. (1)

Fig. A-1 presents an arbitrary control volume V undergoing a phase change. In the volume V the total enthalpy H can be written as the sum of sensible enthalpy h and latent heat Δh_m, i.e.

$$H = h + \Delta h_m = c_p T + \Delta h_m. \tag{A-1}$$

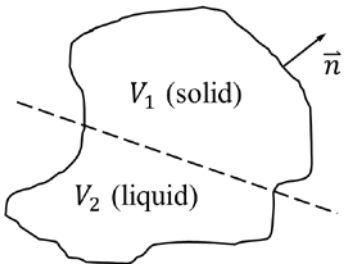

Fig. A-1 An arbitrary control volume.

Based on the volume V an energy balance will give

$$\frac{\mathrm{d}}{\mathrm{d}t}\int_V \rho H \mathrm{d}V = \int_S -\rho H \vec{u}\cdot\vec{n}\mathrm{d}S + \int_S \lambda \nabla T\cdot\vec{n}\mathrm{d}S, \tag{A-2}$$

where $V = V_1 + V_2$; S is the surface area; $\vec{u}$ is the velocity; and $\vec{n}$ is the normal vector of external surface. Appling a divergence theorem, Eqn. (A-2) becomes

$$\int_V \left[\frac{\partial(\rho H)}{\partial t} + \nabla\cdot(\rho H\vec{u}) - \nabla\cdot(\lambda\nabla T)\right]\mathrm{d}V = 0. \tag{A-3}$$

Since V is arbitrary and if the flow is negligible, Eqn. (A-3) can be expressed as

$$\frac{\partial(\rho H)}{\partial t} - \nabla\cdot(\lambda\nabla T) = 0. \tag{A-4}$$

Combining Eqns. (A-1) and (A-4) yields

$$\frac{\partial\left(\rho c_p T\right)}{\partial t} = \nabla\cdot(\lambda\nabla T) - \frac{\partial(\rho\Delta h_m)}{\partial t}. \tag{A-5}$$

which can be easily transformed into Eqn. (1) for the PCMs region under a spherical coordinates system with spherical symmetry.

B. Derivation of Eqn. (7)

The Gibbs free energy $g_j(T_m, P)$ can be estimated by a second order Taylor expansion around $g_{j0}(T_{m0}, P_0)$:

$$\begin{aligned} g_j(T_m, P) = g_{j0} &+ \left.\frac{\partial g_j}{\partial T_m}\right|_{P_0}(T_m - T_{m0}) + \left.\frac{\partial g_j}{\partial P}\right|_{T_{m0}}(P - P_0) \\ &+ \frac{1}{2}\left.\frac{\partial^2 g_j}{\partial T_m^2}\right|_{P_0}(T_m - T_{m0})^2 + \left.\frac{\partial^2 g_j}{\partial P^2}\right|_{T_{m0}}(P - P_0)^2 \\ &+ \left.\frac{\partial^2 g_j}{\partial T_m \partial P}\right|_{P_0, T_{m0}}(T_m - T_{m0})(P - P_0), \end{aligned} \tag{B-1}$$

The Gibbs relation based on Gibbs free energy is defined as [30]

$$\mathrm{d}g_j = -s_j \mathrm{d}T_m + \frac{1}{\rho_j}\mathrm{d}P \tag{B-2}$$

which combined with the fundamental relation for the total differential yields

$$\left.\frac{\partial g_j}{\partial T_m}\right|_P = -s_j, \ \left.\frac{\partial g_j}{\partial P}\right|_{T_m} = \frac{1}{\rho_j}. \tag{B-3}$$

The differential relationship of the entropy can be written as [30]

$$\mathrm{d}s_j = \frac{c_{pj}}{T_m}\mathrm{d}T_m - \left.\frac{\partial\left(1/\rho_j\right)}{\partial T_m}\right|_P \mathrm{d}P, \tag{B-4}$$

which similarly yields

$$\left.\frac{\partial s_j}{\partial T_m}\right|_P = \frac{c_{pj}}{T_m}. \tag{B-5}$$

The thermal expansion coefficient and isothermal compressibility are defined as [30]

$$\alpha_j = \rho_j \left.\frac{\partial\left(1/\rho_j\right)}{\partial T_m}\right|_P, \ \beta_j = -\rho_j \left.\frac{\partial\left(1/\rho_j\right)}{\partial P}\right|_{T_m}. \tag{B-6}$$

Based on Eqns. (B-3), (B-5) and (B-6), we get

$$\begin{cases} \left.\frac{\partial^2 g_j}{\partial T_m^2}\right|_P = -\left.\frac{\partial s_j}{\partial T_m}\right|_P = -\frac{c_{pj}}{T_m}, \\ \left.\frac{\partial^2 g_j}{\partial P^2}\right|_{T_m} = \left.\frac{\partial\left(1/\rho_j\right)}{\partial P}\right|_{T_m} = -\frac{\beta_j}{\rho_j}, \\ \left.\frac{\partial^2 g_j}{\partial T_m \partial P}\right|_{P,T_m} = \left.\frac{\partial\left(1/\rho_j\right)}{\partial T_m}\right|_P = \frac{\alpha_j}{\rho_j}. \end{cases} \tag{B-7}$$

By reporting Eqns. (B-3) and (B-7) in Eqn. (B-1), Eqn. (7) is derived.